Systematical Characterization of Material Response to Microscale Laser Shock Peening

Hongqiang Chen
Youneng Wang
Jeffrey W. Kysar
Y. Lawrence Yao

Department of Mechanical Engineering,
Columbia University,
New York, NY 10027

The response of materials after microscale laser shock peening (μLSP) was experimentally characterized and compared with the theoretical prediction from FEM analysis in microlength level. Since μLSP is predominantly a mechanical process instead of a thermal process, the characterization focuses on mechanical properties and associated microstructures. An X-ray microdiffraction technique was applied on the postpeened single crystal aluminum of (001) and (110) orientations, and an X-ray profile was analyzed by subprofiling and Fourier analysis method. Spatially resolved residual stress and strain deviation was quantified and explained in terms of the heterogeneous dislocation cell structure. In-plane crystal lattice rotation induced by μLSP were measured by electron backscatter diffraction (EBSD) and compared with the FEM simulation. Average mosaic size was evaluated from X-ray profile Fourier analysis and compared with the result from EBSD. Surface strength increase and dislocation cell structure formation were studied. The systematical characterization helps develop more realistic simulation models and obtain better understanding in microlength level. [DOI: 10.1115/1.1811115]

Keywords: Laser Shock Peening, Single Crystal Aluminum, X-ray Microdiffraction, Residual Stress

1 Introduction

In recent decades, failure and reliability of MEMS has been drawing increasing attention [1–2]. Fatigue behavior, for instance, may ultimately limit product lifetime in applications, such as microengines and microswitches. One will find needs to impart a desirable residual stress distribution or alter the existing distribution left by the fabrication process itself. Microscale laser shock peening (μLSP) is a technique that can potentially be applied to manipulate the residual stress distribution in surface layers of metal structures with micron-level spatial resolution and thus enhance fatigue and reliability performances of microdevices [3].

Microscale laser shock peening of polycrystalline aluminum and copper has been studied and shown to significantly improve fatigue performance of the peened targets due to the compressive residual stress [4–6]. Compared with mechanical shot peening, the compressive stresses extend much deeper below the surface and the resulting fatigue life enhancement is often greater. It has also been shown through FEM simulation results that μLSP efficiently induces favorable residual stress distributions in metal targets. To fully understand the effect of μLSP and validate the FEM result, X-ray diffraction was used to measure average residual stress and/or strain in the depth direction for overlapping shock-peened bulk copper samples [4]. However, the spatial resolution of X-ray diffraction is typically larger than 0.5 mm, which is too large to measure the residual stress and/or strain distributions induced by μLSP [5]. Recently, by using synchrotron radiation sources, X-ray microdiffraction measurements were carried out to obtain stress and/or strain distributions with micron-level spatial resolution. The measurement was based on the intensity contrast method [7,8], in which stress and/or strain in copper thin-film samples was inferred by recording the diffraction intensity contrast of the underlying single-crystal silicon substrate. The result provided qualitative information about the strain field distribution in the shock-peened copper films, but it has proven difficult to quantitatively relate the X-ray diffraction intensity measurements with the stress and/or strain values.

In addition, classical continuum mechanics alone seems to experience difficulty to explain plastic deformation confined to the micron length scale [9]. Thus, in order to comprehensively understand and model the μLSP process, micromechanical considerations and its relationship to crystal structure, crystal lattice orientation, dislocation, and other microstructures under shock wave require consideration. Transmission electron microscopy (TEM) observations of the shock area microstructure were carried out to understand the response to laser shock peening at microlevel [10,11]. However, peened samples needed to be cut to very thin slices for TEM observation, and the experimental result cannot quantitatively characterize the microstructure of the shocked area. Thus, new characterization methods need to be developed to quantitatively measure the microstructure caused by μLSP.

In this paper, the spatially resolved X-ray diffraction profiles from microscale laser shock-peened bulk single-crystal aluminum of different crystalline orientations (001 and 110) were recorded at the microscale. The spatial distribution of residual stress and/or strain, strain deviation, and mosaic size induced in μLSP were subsequently quantified. Crystal lattice rotation caused by plastic deformation during high strain-rate laser shock peening was measured by electron backscatter diffraction (EBSD). The experimental results were then compared with that of simulations obtained from FEM analysis based on single-crystal plasticity. Thus, these measurements provide the possibility to study the response of materials to laser shock peening at the microscale and can be used to verify the results of FEM analysis as well.

2 Experiment and Simulation Conditions

2.1 Microscale Laser Shock-Peening (μLSP) Experiment Conditions. As illustrated in Fig. 1, a frequency tripled Q-switched Nd:YAG laser ($\lambda = 355$ nm) in TEM_{00} mode was used in the μLSP experiments because of higher laser-energy absorption on aluminum samples at shorter wavelengths. The pulse duration was 50 ns, spacing between consecutive pulses along a shock line was 25 μm, and pulse numbers were 3 on each shocked

Contributed by the Manufacturing Engineering Division for publication in the JOURNAL OF MANUFACTURING SCIENCE AND ENGINEERING. Manuscript received February 01, 2004; revised August 02, 2004. Associate Editor: K. Dohda

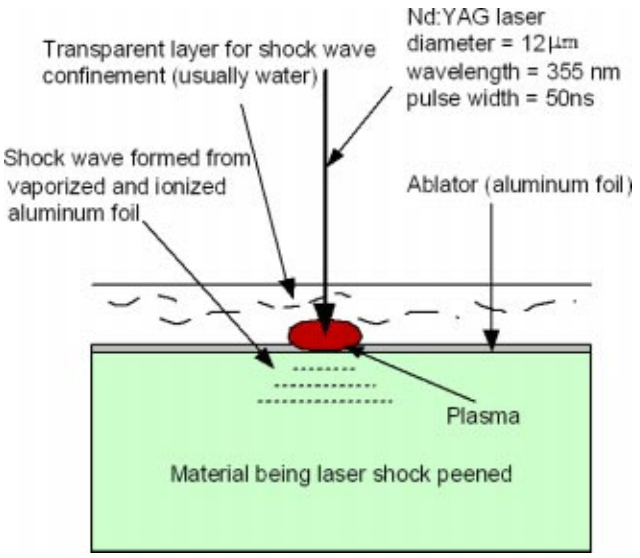

Fig. 1 Laser shock-peening process

location at 1 KHz pulse repetition rate. Laser beam diameter was 12 μm and laser intensity was approximately 4 GW/cm^2. A thin layer of high-vacuum grease (about 10 μm thick) was spread evenly on the polished sample surface, and a 16 μm thick polycrystalline aluminum foil, chosen for its relatively low threshold of vaporization, was tightly pressed onto the grease. The sample was placed in a shallow container filled with distilled water around 3 mm above the sample's top surface. After μLSP, the coating layer and the vacuum grease were manually removed. The induced deformation is due to shock pressure and not due to thermal effects, since only the coating is vaporized by the laser shock. Further details of μLSP setup are given to [4–6].

Fully annealed single crystals of pure aluminum with orientations (001) and (110), shown in Fig. 2, were used for μLSP experiments. Aluminum is one of materials routinely used in microdevices due to its good mechanical and electrical properties. Although polycrystalline metals are more widely used in practice, single crystal metal is ideal for fundamental study. The sample was cut to shape using wire electrical discharge machining (EDM). A Laue X-ray was used to determine the crystal orientation within $\pm$1 deg and laser shock peening was applied along this

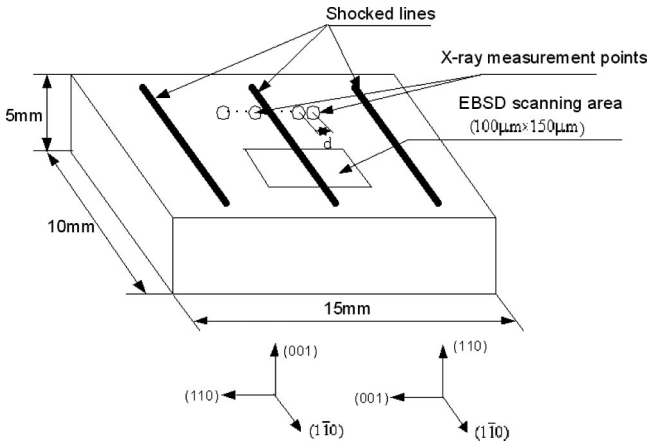

Fig. 2 Sample geometry and laser shock-peening condition (X-ray measurement points are along a line perpendicular to a shocked line and within $\pm$100 μm from the center of a shocked line, d=5 μm, within $\pm$20 μm from the shocked line center, d =10 μm, elsewhere; EBSD scan area is 100 μm×150 μm).

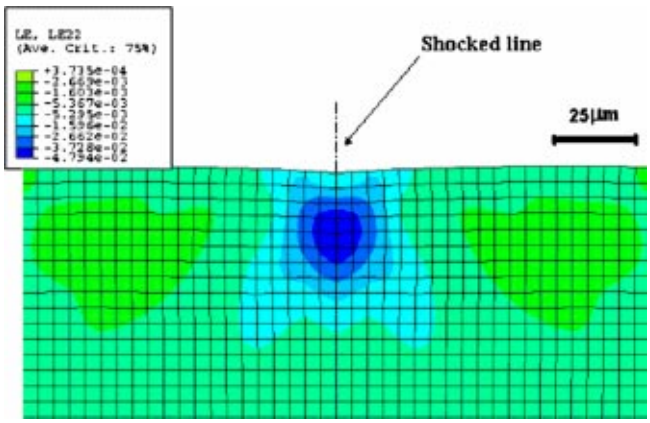

Fig. 3 Typical FEM simulation result of strain distribution in depth direction, Al (001) sample: 200×80 μm as shown; total simulation region is 800×400 μm, deformation factor=5 for viewing clarity.

direction in all samples. Regular mechanical polishing with diamond grit sizes 6 and 1 μm was used to remove the heat-affected zone of the cutting surface, and electrochemical polishing was applied for all samples to eliminate any remaining deformed material prior to shock peening.

2.2 FEM Simulation Conditions. In FEM analysis, the spatial and temporal dependent shock pressure was solved numerically based on Ref. [12] and was extended to a spatial nonuniform shock pressure with a Gaussian spatial distribution [4–5]. The nonuniform shock pressure was then used as the loading for the subsequent stress and/or strain analysis, in which von Mises criterion was used, and the analysis was implemented in a commercial solver, ABAQUS. Based on the theory of Asaro [13], a user-material subroutine UMAT for single-crystal plasticity written by Huang [14] and modified by Kysar [15] is incorporated into the finite element analysis [16]. In the UMAT, the $\{111\}\langle 110\rangle$ slip systems in FCC metal are used for single crystal Al. A critical shear strength $\tau_{CRSS}=1$ MPa on each of the slip systems is assumed. The induced deformation state is two-dimensional, i.e., a plane strain deformation state, with the experiment conditions indicated in Fig. 2, according to Rice [17]. Simulation was carried out in two-dimensional and finite geometry (800 μm in length and 400 μm in height) was assumed. Shocks are applied on the top surface along a narrow strip in the width direction. The bottom surface is fixed in position, while all the other side surfaces are set traction free. In order to eliminate the ''volume locking'' that oc-

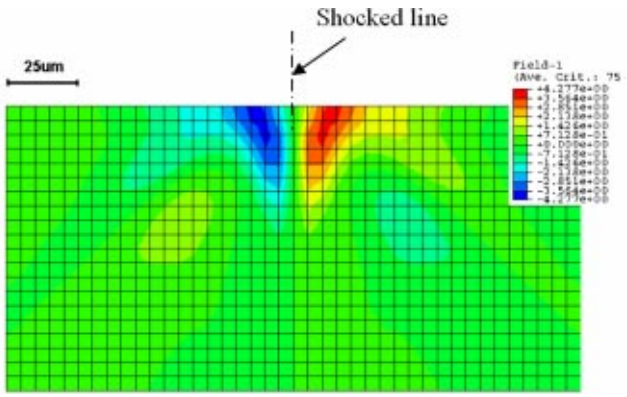

Fig. 4 Typical lattice rotation field on cross section after laser shock peening, Al (110) sample: 200×100 μm as shown; total simulation region is 800×400 μm.

curs in plastic deformation simulation, linear elements with reduced integration and hourglass stiffness control are used. With the FEM model based on single-crystal plasticity, material response at either macroscale or microscale can be predicted, such as geometry deformation, residual stress and/or strain spatial distribution, and lattice rotation field. Figures 3 and 4 show the typical simulation results of strain distribution and lattice rotation field in cross section for sample Al (001) and Al (110), respectively. However, it is necessary to verify the predications and optimize parameters of the FEM model by experiments both in the macro- and microlevels.

3 Measurement and Characterization Methods

3.1 X-ray Microdiffraction Measurement. A high-brightness X-ray beam (beamline X20A) of National Synchrotron Light Source at Brookhaven National Lab was used in diffraction, and the beam size was 5 by 7 μm. Monochromatic synchrotron radiation at 8.0 KeV ($\lambda = 1.54024$ Å) was used, since it is smaller than the *K* absorption edge for Al, which is 8.98 KeV [18], so that the fluorescence radiation would not be excited. To obtain a proper 2θ diffraction profile for each measurement point, the diffraction conditions of the two Euler angles of θ and χ angles should be optimized for every measuring point. The optimization of θ and χ is to set the normal of the diffracting planes at the proper orientation on the diffractometer [19].

Multiple measurement points were chosen along a line perpendicular to a shocked line as shown in Fig. 2. The spacing between adjacent measurement points starts from 10 μm (when ± 100 μm away from the center of the shocked line) and reduces to 5 μm within ± 20 μm from the center of the shocked line in order to spatially resolve the residual stress, as shown in Fig. 2. At each position, the corresponding X-ray diffraction profile is recorded by a modified version of the SPEC software package [20] and repeated for each shocked line.

3.2 EBSD Measurement. In addition to X-ray microdiffraction, electron backscatter diffraction (EBSD), a technique for obtaining crystallographic orientation with submicron spatial resolution was applied to the shock-peened samples. Microstructure changes, such as crystallographic orientation and texture, were studied quantitatively. EBSD data were collected using a system supplied by HKL Technology [21] and attached to a JEOL JSM 5600LV scanning electron microscope (SEM). The samples were briefly electrically polished to remove the mechanical scratches on the surface. The shocked region was accurately located using SEM before the EBSD measurements. All data were acquired in the automatic mode, using external beam scanning and employing a 1 μm step size. The scan area is 100 μm$\times$150 μm on the shocked surface and covered the shocked line center as shown in Fig. 2. Details about EBSD measurement can be found in [22].

3.3 Spatially Resolved Residual Strain/Stress Evaluation Method. If a piece of metal is deformed elastically such that the strain is uniform over a relatively large distance, the uniform macrostrain will cause a shift in the diffraction lines to new positions. If the metal is deformed plastically, such as in this case, the deformation creates adjacent regions of slight different orientations. The residual strain can vary from region to region to cause a nonhomogeneous strain state, which results in strain deviation and a broadening of the diffraction profile. In fact, both kinds of strain are superposed in plastically deformed metals, and diffraction is both shifted and broadened [18]. It is the superposition that makes it difficult to evaluate the local strain and residual stress distribution.

However, on the basis of a composite model, local strain and residual stress can be evaluated for single-crystal metal under plastic deformation as reported by Ungar [23] by recognizing that the crystal dislocations often arrange themselves in a cell structure. A cell structure consists of ''cell interior'' and ''cell wall'' as postulated by [23]. The cell walls parallel to the compressive axis are under a residual uniaxial compressive stress $\Delta\sigma_w < 0$ and the cell interior under a uniaxial tensile stress $\Delta\sigma_c > 0$. The asymmetrical Bragg reflections can then be separated into the sum of two symmetrical peaks, which correspond to cell interior and cell wall. For brevity, the subscripts *w* and *c* will be used for walls and cell interiors respectively. The integral intensities of the subprofiles relative to the integral intensity of the measured profile are proportional to the volume fractions of the cell walls f_w and cell interiors $f_c = 1 - f_w$, respectively. According to the model, stress equilibrium of the unloaded crystal requires

$$f_w \Delta\sigma_w + (1 - f_w)\Delta\sigma_c = 0 \tag{1}$$

The asymmetric line profiles I are assumed to be composed of two components I_w and I_c, where I_w is attributed to the cell-wall material (the integral intensity of which is proportional to f_w) and I_c to the cell-interior material [the integral intensity of I_c is proportional to $f_c = (1 - f_w)$]. The centers of both components are shifted in opposite directions in accordance with $\Delta\sigma_w < 0$ and $\Delta\sigma_c > 0$. These shifts can be expressed by the relative change of the mean lattice plane spacing $\Delta d/d$ as follows:

$$\left.\frac{\Delta d}{d}\right|_w = \frac{\Delta\sigma_w}{E} < 0, \quad \left.\frac{\Delta d}{d}\right|_c = \frac{\Delta\sigma_c}{E} > 0 \tag{2}$$

where E is Young's modulus. We introduce a Cartesian coordinate system with the *z*-axis parallel to the stress axis and the *x*- and *y*-axes perpendicular to the two sets of walls that are parallel to the stress axis. Then, the measure of the residual stresses can be characterized by the absolute value of the difference

$$\sigma_{zz} = |\Delta\sigma_w - \Delta\sigma_c| \tag{3}$$

Their range of influence is of the order of the cell dimensions, which is longer than the range of individual dislocations in a random distribution, (e.g., in cell walls or in cell interiors). The lateral residual stress in the sample surface plane is

$$\sigma_{xx} = \sigma_{yy} = -\sigma_{zz} \cdot \nu \tag{4}$$

where υ denotes Poisson's ratio.

3.4 Strain Deviation and Mosaic Size-Evaluation Method. Based on the Fourier analysis of the diffraction profiles, the Warren and Averbach method [24] allows to obtain strain deviation and distribution function of mosaic size directly from the Fourier series coefficients.

Considering a single-crystal sample in which there is plastic deformation induced by laser shock peening, there is nonuniform spacing change between the diffraction planes in a region and strain variation is thus induced, causing a broadening of the X-ray line profile. The shock peening also produces dislocation arrays [23,25], such as small angle boundaries that subdivide the original single crystal into small coherent domains as grains in polygrained metal. As a result, the peened region can be regarded as polygrained metal [26]. Those small mosaics, such as grain, will cause the broadening of the line profile because there are not as many planes to cause destructive interference away from the exact Bragg angle [18]. Therefore, both kinds of effects contribute to the broadening of the X-ray line profile in plastically deformed metals.

From the analysis of [24], the sample can be represented as columns of unit cells along the direction that is perpendicular to the diffraction plane in the reciprocal lattice space. The X-ray line profile can be considered as the combination of reflected X-ray from all pairs of unit cells. The measured X-ray line profile is then represented as the Fourier series in the reciprocal lattice space [24]

$$P(2\theta) = \frac{KNF^2}{\sin^2\theta} \sum_{n=-\infty}^{+\infty} (A_n \cos 2\pi nh + B_n \sin 2\pi nh) \tag{5}$$

where $P(2\theta)$ represents the measured X-ray line profile versus 2θ, F is the structure factor and K is the angular factor. N represents the number of unit cells in the sample and h is the reciprocal of the lattice spacing. The real part of Fourier coefficient A_n can be described as the product of the size effect and the strain effect [27]:

$$A_n = A_n^S A_n^D \tag{6}$$

where A_n^D represents the spacing change between the diffraction planes and A_n^S is a measure of the grain size. Furthermore, for small values of l and n, A_n can be expressed by [27]

$$\ln A_n = \ln A_n^S - 2\pi^2 l^2 n^2 \langle \varepsilon^2 \rangle \tag{7}$$

where l is the number of unit cells between diffraction planes and $\langle \varepsilon^2 \rangle^{1/2}$ is standard strain deviation that indicates strain uncertainty. According to Eq. (7), $\ln A_n$ versus n^2 is represented as a straight line, whose slope and intersection with $n=0$ can be used to evaluate the strain deviation and size effects.

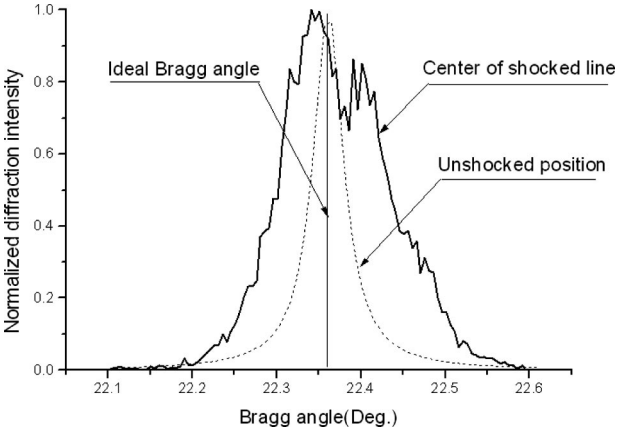

Fig. 6 Two cross sections of Fig. 7 measured at position at the center of shocked line and at unshocked position (100 μm away from the shock line center)

4 Results and Discussions

As mentioned before, after shock peening, macroscopic quantities (residual strain and stress), and microscopic quantities (crystalline orientation field and mosaic size) can be evaluated through the analysis method based on the data from X-ray microdiffraction or EBSD measurement in Sections 3.1 and 3.2, and compared with the FEM simulation.

4.1 Macroscopic Quantities

4.1.1 Spatially Resolved Residual Stress Characterization Figures 5 and 7 show the three-dimensional spatial distribution of those measured X-ray profiles for Al (002) and (220) reflection in the direction perpendicular to the shocked line, respectively. The corresponding X-ray profiles at the shock-peened center and unshocked region are singled out in Figs. 6 and 8 to show the noted difference. It is clear that after shock peening, the X-ray profile was significantly broadened and became asymmetric compared to the unshocked region for both (001) and (110) samples. Considering the X-ray profile of the (001) sample at 5 μm, to the right of the shocked line center as shown in detail in Fig. 9, the raw profile represented by the unsmoothed curve is smoothed to obtain the fitted profile I, which is subsequently decomposed into two symmetric subprofiles I_c and I_w using the Lorentzian peak function [27]. The centers of the decomposed subprofiles are found to be shifted in opposite directions and the shifts can be related to the relative change of the mean lattice plane spacing $\Delta d/d$ of the corresponding lattice planes

$$\left.\frac{\Delta d}{d}\right|_{c(\text{or } w)} = -\cot\theta \Delta\theta_{c(\text{or } w)} \tag{8}$$

where $\Delta\theta_{c(\text{or } w)}$ is the angular shift of the subprofiles I_c (or I_w) relative to the exact Bragg angle θ of the shock-free regions. This equation is based on taking total differential of the Bragg law assuming a perfect X-ray wavelength. For Al (002) reflection profile at position $+5$ μm from the shocked line, the ideal Bragg angle corresponding to the shock-free regions is θ=22.36 deg, the centers of gravity of the decomposed subprofiles are θ_c=22.328 deg, and θ_w=22.388 deg, and therefore, $\Delta\theta_c = -0.032$ deg and $\Delta\theta_w$=0.028 deg. For Al crystals with $E=70$ GPa and $\upsilon=0.33$, $\Delta\sigma_c$ and $\Delta\sigma_w$ are 95 MPa and -82.6 MPa, respectively, according to Eqs. (2) and (8). Equation (3) gives the axial residual stress σ_{zz}=177.6 MPa, and Eq. (4) gives the lateral residual stress within the sample surface plane

$$\sigma_{xx} = \sigma_{yy} = -\sigma_{zz} \cdot \nu = -58.6 \text{ MPa} \tag{9}$$

Following the analysis method above for each measurement point, the spatially resolved residual stress distribution for Al (001) is shown in Fig. 10. The simulation results from FEM are also overlapped in Fig. 10. The distributions show similar patterns and

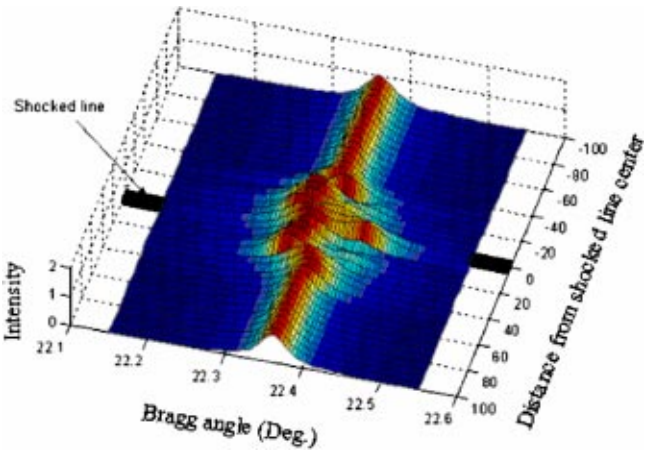

Fig. 5 3D X-ray profile spatial distribution across the shocked line for (002) reflection of Al (001) sample [24] (*x*-axis: distance from the shocked line center (μm); *y*-axis: Bragg angle (deg); and *z*-axis: normalized diffraction intensity)

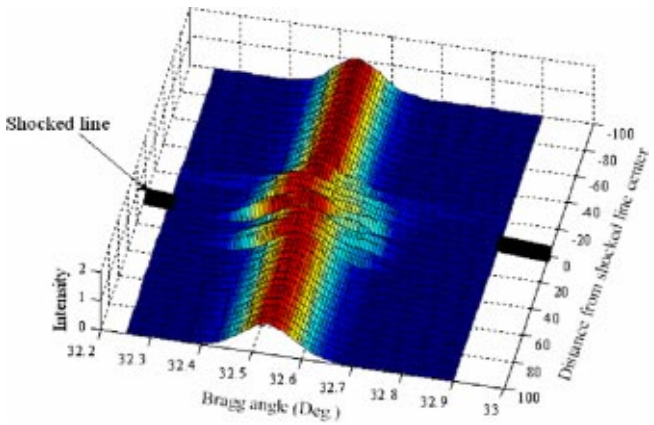

Fig. 7 3D X-ray profile spatial distribution across the shocked line for (220) reflection of Al (110) sample (*x*-axis: distance from the shocked line center (μm); *y*-axis: Brag angle (deg); and *z*-axis: normalized diffraction intensity)

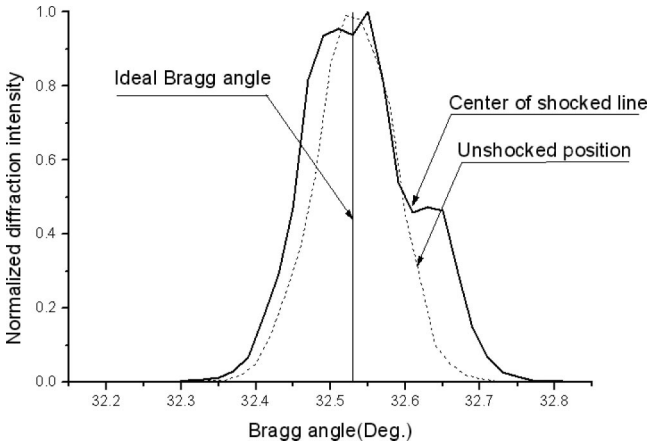

Fig. 8 Two cross sections of Fig. 6 measured at position at the center for shocked line, and at unshocked position (100 μm away from the shock line center)

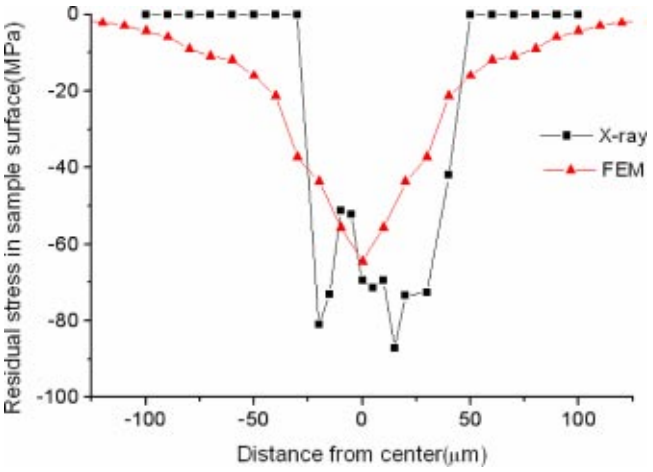

Fig. 10 Typical spatial distribution of residual stress in Al (001) sample surface by X-ray diffraction measurement and FEM simulation

generally agree with each other. In terms of the lateral extent of the compressive residual stress, the experiment results indicate about ± 40 μm from the center of shocked line, while FEM results overestimate it. This is likely due to the shock pressure model used in the FEM, which may have overestimated the lateral expansion effect of pressure loading on the sample surface [4].

4.1.2 Strain Deviation Spatial Distribution Across the Shocked Region. To better understand shock-induced plastic deformation, it is necessary to study the corresponding inhomogeneous strain variation in the depth direction, which can be calculated from the recorded X-ray profiles according to the method discussed in Section 3.4. From the theory of [24], for small values of l and n, the logarithm of the measured Fourier coefficient is given by Eq. (7). For Al (002) reflection, $l=2$, so the strain effect term can be represented as $-2\pi^2 l^2 n^2 \langle \varepsilon_l^2 \rangle$, in which $\langle \varepsilon_l^2 \rangle^{1/2}$ represented standard strain deviation caused by the laser shock peening in the [002] direction, which is in the depth direction perpendicular to the surface for Al(001) sample. If we choose n^2 as the x-axis and $\ln A_n(l)$ as the y-axis, Eq. (7) represents a straight line with slope $K=-2\pi^2 l^2 \langle \varepsilon^2 \rangle$. Thus, the slope of this fitted line can be used to calculate the strain deviation from that X-ray profile as

$$\langle \varepsilon_l^2 \rangle^{1/2} = \sqrt{\frac{K}{-2\pi^2 l^2}} \tag{10}$$

For example, at the position of 10 μm from the shocked line, the slope of fitted line is $K=-0.05035$, $l=2$ for Al (002) reflection, so the $\langle \varepsilon_l^2 \rangle^{1/2}$ is 0.025 based on Eq. (10). In order to obtain the spatial distribution of the strain deviation in depth direction, X-ray profiles at each position cross the shocked line (from 30 μm left of the shocked line to 30 μm on the right) were processed by using Fourier transformation with Stoke's correction [27]. Fourier number n^2 versus $\ln A_n$ for sample Al (001) is shown in Fig. 11

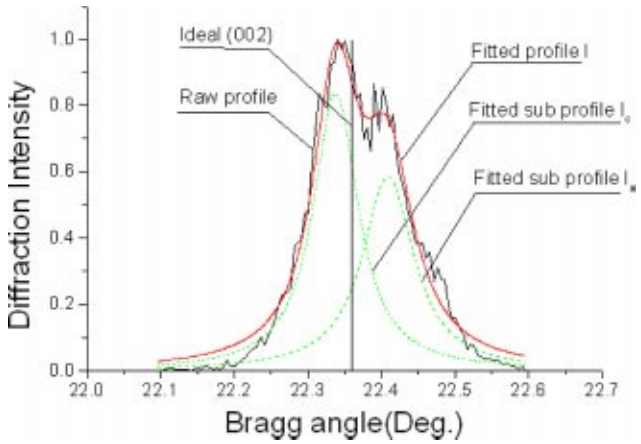

Fig. 9 Detailed view of decomposition of an asymmetric line profile into the sum of two symmetric subprofiles, diffraction intensity normalized (subprofile I_c: cell interior; and subprofile I_w: cell wall)

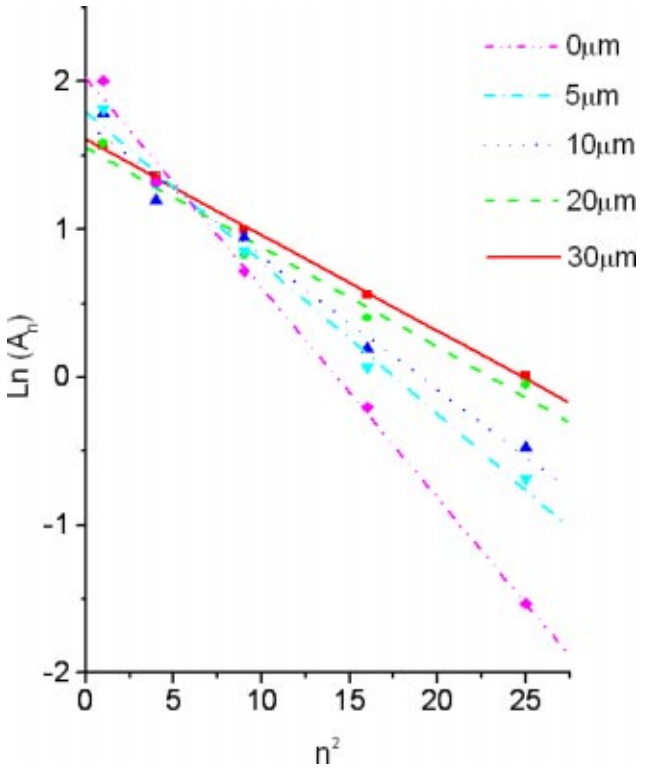

Fig. 11 $\ln(A_n)$ versus n^2 lines at different position from the center of shocked line for Al (002) reflection [27] (A_n: the real part of corrected Fourier coefficient; and n: Fourier series number)

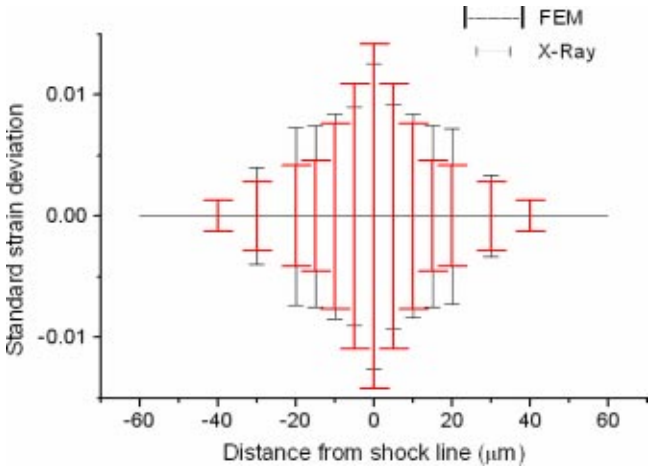

Fig. 12 Standard strain deviation in depth direction by Fourier transformation and FEM simulation for sample (001)

[28]. It is clear that the magnitude of line slope increases from the position far away from the shock line center (30 μm) to the center of shock line (0 μm). So it shows the strain deviation increases gradually when the position moves closer to the shocked center. Figure 12 shows the spatial distribution of strain deviation in the depth direction for Al (001) sample by Fourier analysis. For FEM simulation, the corresponding standard deviation of strain at each point was obtained by considering the effective penetration depth of the X-ray. Choosing the depth of 90% of the total diffracted intensity

$$x = \frac{2.3 \times \sin \theta_0}{2\mu} \tag{11}$$

where θ_0 is ideal Bragg angle and μ is the linear absorption coefficient, the effective depth is 45 μm for single-crystal aluminum (110) with $\theta_0 = 32.53$ and $\mu = 135.6\ \text{cm}^{-1}$ [18]. In this surface layer of depth 45 μm, nine values of strain were obtained, since spacing between adjacent notes is 5 μm in the depth direction. Thus, the standard strain deviation for FEM simulation is

$$SD = \sqrt{\frac{\sum_{i=1}^{n} (\varepsilon_i - \bar{\varepsilon})^2}{n-1}} \tag{12}$$

where n is the sample size, $\bar{\varepsilon}$ is the average strain at each point (shown in Fig. 12). As seen in the Fig. 12, the maximum strain deviation levels can be found in a region of ± 20 μm from Fourier analysis of the X-ray profile, which is in good agreement with the result from FEM simulation.

4.2 Microscopic Quantities

4.2.1 Crystal-Lattice Rotation. Crystal-lattice rotation is well defined within the context of kinematics of single-crystal plasticity and a key parameter in the simulation model. It is well known [17] that both face-centered cubic (*fcc*) and body-centered cubic (*bcc*) crystals admit a state-of-plane strain deformation if the crystal is oriented and the mechanical loading is applied along certain crystallographic directions. The current orientation of the lattice directions with respect to the initial one is determined by the rotation in the polar decomposition of the elastic part of deformation [29]. Therefore, the crystalline orientation field measured from EBSD enables characterization of the in-plane lattice rotation induced by microscale laser shock peening under approximate plane strain conditions to compare with the results from the FEM analysis.

The lattice rotation contour map on the shocked Al (001) sample's surface is shown in Fig. 13(*a*). Figure 13(*b*) shows the spatial distribution of lattice rotation along two lines across the shocked line with spacing$=34$ μm. The red region corresponds to counterclockwise rotation about the z-axis, which is positive; and the blue region corresponds to clockwise rotation, which is negative. It is clear to see that the lattice rotation is zero (green region) far away from the shocked line, which corresponds to the shock-free region. The lattice-rotation distribution along the shocked line is quite similar along two lines, which suggests the approximate two-dimensional deformation state. The lattice rotation value is ± 3 deg between ± 35 μm from the center of shocked line, and the rotation direction is antisymmetric on both sides of shocked line. In order to investigate the effect of crystal orientation on lattice rotation, an aluminum sample shocked on the (110) surface was also studied as seen in Figs. 14(*a*) and (*b*). The general trend of lattice rotation, such as the rotation direction and magnitude, is the same with that of Al (001).

Simulation for spatial distribution of lattice rotation was carried out and shown in Fig. 15. It can be seen that the lattice rotation distribution is quite similar to the experimental results. When the position changes from left of shock line to the right for Al (011), the lattice rotation starts from zero deg (beyond ± 40 μm) to a maximum negative value (-4 deg at -15 μm) and after that, the

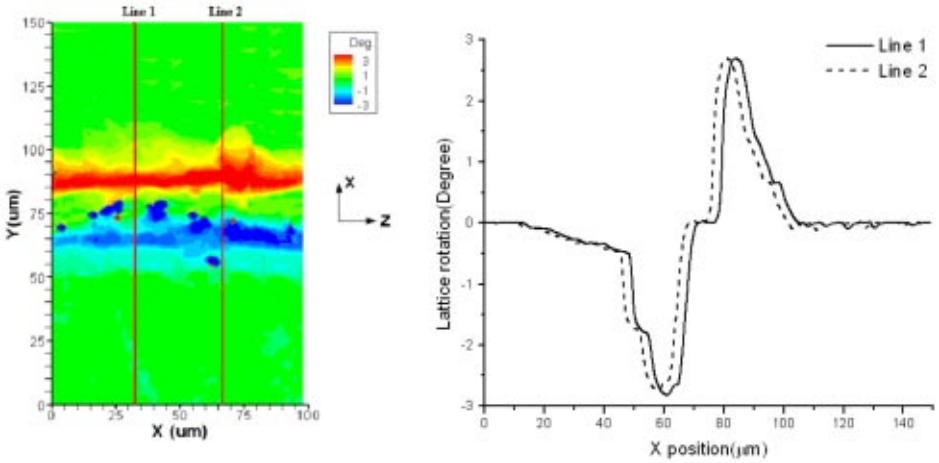

Fig. 13 Lattice rotation contour map on sample surface for Al (001) sample (line 1–2: two cross sections with spacing$=34$ μm)

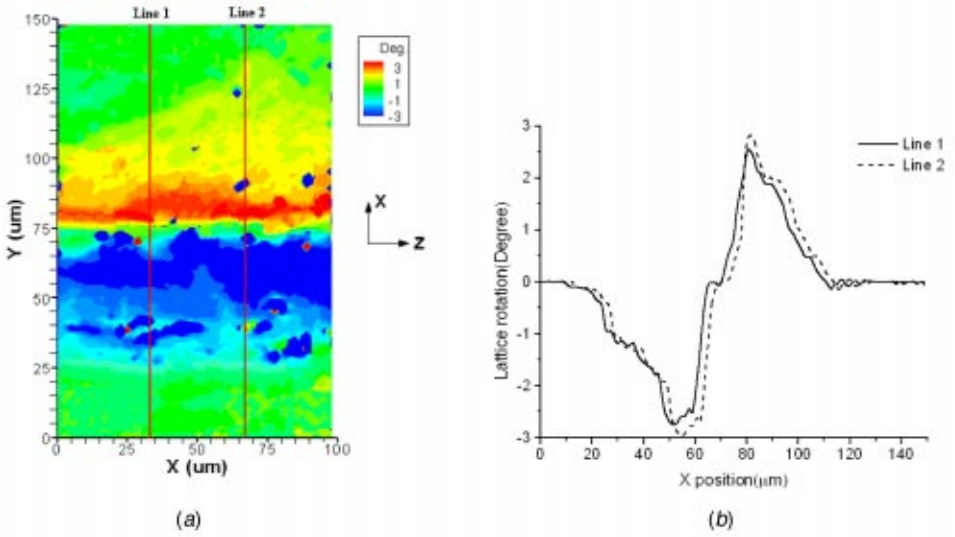

Fig. 14 Lattice rotation contour map on sample surface for Al(110) sample (line 1–2: two cross sections with spacing=34 μm)

magnitude of lattice rotation decreases to zero again close to the shocked line center. For the right side of shock line center, the distribution is antisymmetric with the left side.

4.2.2 Average Mosaic Size. As discussed before, the size-broadening effect is represented by a cosine Fourier series similar to that developed for strain broadening, and, hence, the Fourier coefficients A_n give very general method of handling either effect. From the analysis of [24], the initial slope of the A_n versus n curve is

$$\left(\frac{dA_n}{dn}\right)_{(n=0)} = -\frac{1}{\overline{N}_3} \tag{13}$$

where $\overline{N}_3 a_3$ is the average column length, and, hence, an average mosaic size in the direction a_3. Also we have

$$1/2=(2a_3/\lambda)(\sin\theta-\sin\theta_0) \tag{14}$$

where λ is the wavelength of the X-ray, θ is the maximum angle in the X-ray profile, and θ_0 is the ideal Bragg angle. So if the size-broadening effect is expressed in terms of a plot of the Fourier coefficients A_n versus n, the initial slope of the curve gives directly the average column length, which is the average mosaic size in that direction.

Figure 16 shows the initial slope of the A_n versus n curve (the line connecting the first two points in A_n-n curve) at different distance from the shock line center. If the initial slope of curve is K, then the average mosaic size D at that position can be evaluated as

$$D=\left(\frac{1}{K}\right)\cdot a_3 \tag{15}$$

From the analysis above, the size effect can be obtained from Fourier analysis of X-ray profiles. Figure 17 shows the spatial distribution of average mosaic size for Al (110) sample evaluated from the X-ray profile analysis mentioned above. It can be seen that the average mosaic size decreases when move closer to the shock line center. In the region of ± 20 μm from the center, the mosaic size is around 1 μm to 0.7 μm and increases sharply to over 100 μm beyond this range. This is reasonable because the

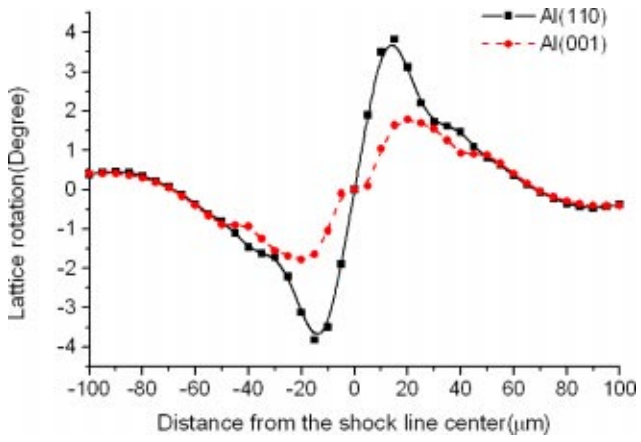

Fig. 15 Spatially distribution of lattice rotation on sample surface from simulation

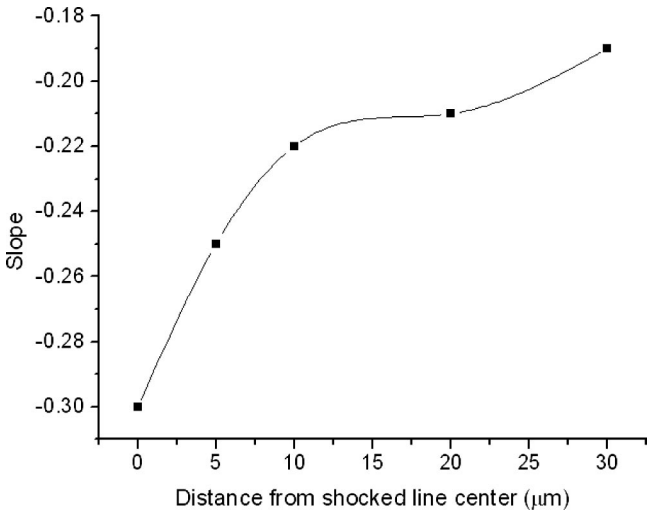

Fig. 16 Initial slope of A_n versus n curves for Al (110) sample

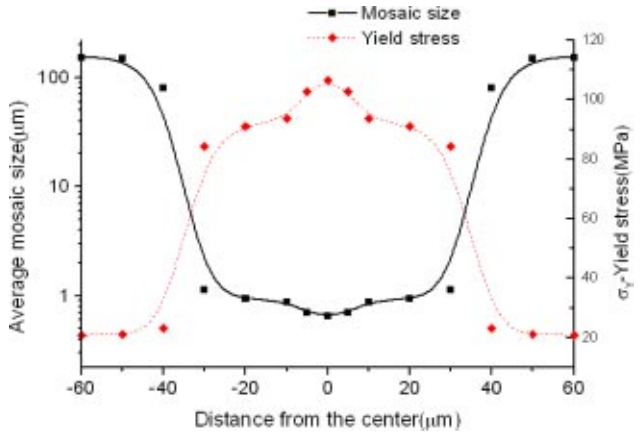

Fig. 17 Spatial distribution of average mosaic size from initial slope analysis by FFT and shock-induced strengthening effects for Al (110)

shock-peening effect is higher in the shock line center, and larger plastic deformation will favor the formation of mosaic structure.

In addition to using X-ray profile analysis to obtain the mosaic size distribution after laser shock peening, EBSD measurement was also applied on sample (110) surface and mosaic structure can be studied directly and compared with the result from the X-ray. Mosaic structures can be quantitatively analyzed through EBSD measurements because EBSD is based on data acquisition of crystalline misorientation angles with submicron spatial accuracy, and the misorientation angle accuracy is less than 1 deg. Figure 18(*a*) shows the microstructures of mosaic for the Al (110) sample. The thin black lines show mosaic boundaries whose misorientation angles are larger than 3 deg. The line *I* represents laser shocked line. The cross sections, represented by lines 1, 2, and 3 with spacing 12.5 μm, are made perpendicular to the shocked line. The spatial distribution of mosaic size along the three lines is shown in Fig. 18(*b*). It is observed that within the shock-peening region (± 20 μm from the shock line center), it has a larger increase in mosaic structure and the smallest mosaic size of 0.8 μm dominant in the center and becomes larger away from the shock-peened region. The result is consistent with the result obtained from the X-ray profile analysis mentioned previously.

As a result of a mosaic size refinement, the shocked area is strengthened according to well-known empirical relationship, such as the Hall-Petch relation between average grain size and the yielding limit of a bulk metal [30], since metal in shocked area can be considered as polycrystalline metal due to the mosaic structure

$$\sigma_Y = \sigma_0 + \frac{k}{\sqrt{d}} \tag{16}$$

where σ_Y is the flow stress, σ_0 and k are material dependent constants, and d is the average mosaic size. For pure aluminum (99.99%), the corresponding σ_0 and k are $\sigma_0 = 15$ MPa and $k = 2.33$ MPa·mm$^{1/2}$ [30]. The yield stress spatial distribution across the shocked area can be obtained by using the average mosaic size and is shown in Fig. 17. It can be seen that strength is improved significantly in shocked area and yield stress is increased to almost 110 MPa in the shocked line center by micro-laser shock peening.

Other than the method of Fourier analysis, average mosaic size can also be roughly estimated by using the Scherrer formula [18]:

$$D = \frac{0.9\lambda}{B \cos \theta_0} \tag{17}$$

where λ = wavelength, B = broadening of diffraction line measured at half its maximum intensity (radians), and θ_0 is the ideal Bragg angle. By using the X-ray profile at 100 μm from the shocked line to correct the instrumental broadening, the calculated average mosaic size is shown in Fig. 19; it shows that the mosaic size is much smaller than the result by Fourier analysis. This is so because X-ray line broadening is relating to the sample and instrument. Sample broadening is usually from mosaic size and inhomogeneous strain variation in d-spacing. The method of the Scherrer formula considers that the total X-ray profile broadening is only caused by the small mosaic size, while Fourier analysis separates the total broadening effect into two parts and calculates mosaic size and strain deviation, respectively. Thus, compared to the result from Fourier analysis, mosaic size of the Scherrer for-

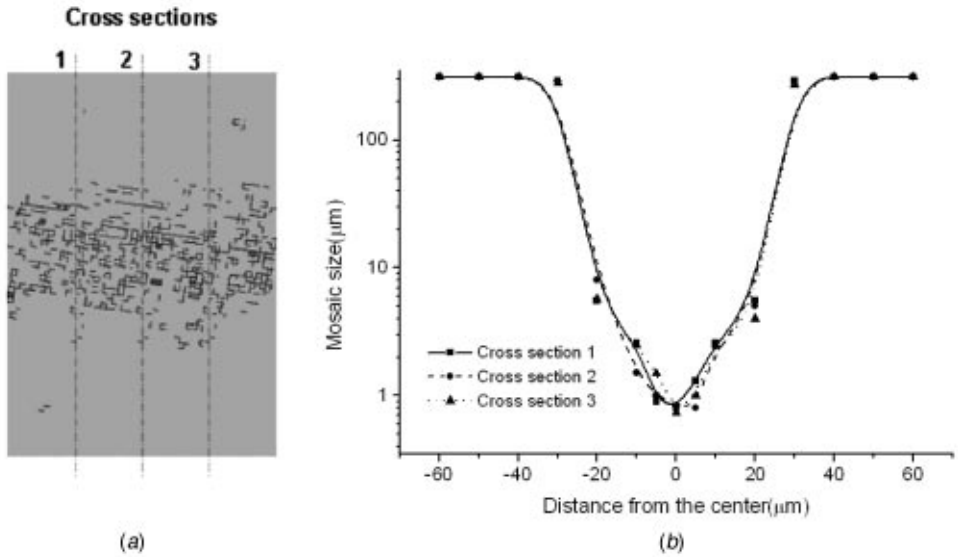

Fig. 18 Mosaic microstructure distribution of Al (110) sample on shocked-peened surface measured with EBSD (50 μm×80 μm). Three cross sections perpendicular to the shocked line are indicated by 1, 2, and 3 [27].

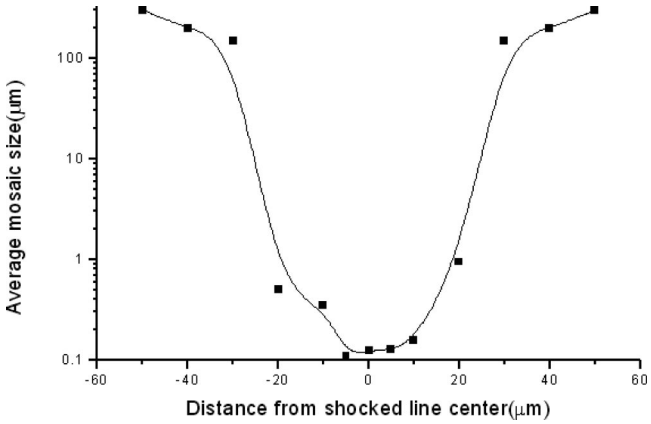

Fig. 19 Spatial distribution of average mosaic size calculated by the Scherrer formula for Al (110)

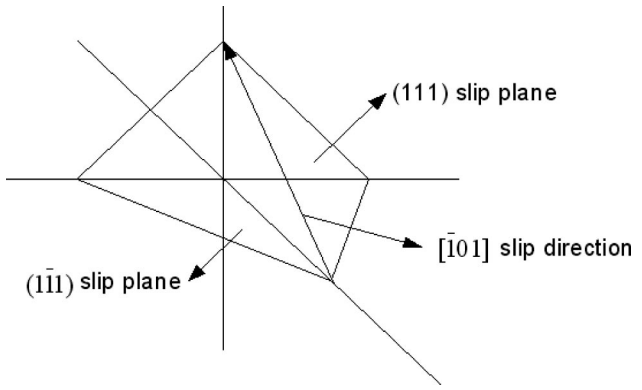

Fig. 21 Cross-slip formation of FCC metal, (111) planes in the ⟨110⟩ directions

mula is smaller. Therefore, Fourier analysis should be used to precisely calculate mosaic size from the recorded X-ray profiles.

4.3 Further Understanding of LSP-Induced Microstructure-Dislocation Cell Structure. From the recorded X-ray profile for the single-crystal Al samples (Figs. 5 and 7), it strongly suggests the existence of dislocation cell structure. In fact, dislocation cell structures were observed via transmission electron microscopy (TEM) in laser shock-peened metals, such as copper [31]. This accompanies the generation and storage of a larger dislocation density during the shock process than for quasi-static processes.

There are various models of dislocation patterning, such as cell structure formation, proposed that differ from the starting point, namely, the driving force of this process [32–34]. According to the thermodynamic approach, dislocation cells are considered as low energy structures [32]. This approach is, however, incorrect because energy minimization principles do not apply to dissipative processes far from equilibrium, such as dislocation glide during plastic deformation. In the synergetic theories developed by [33], the nonlinear dynamics of various dislocation densities is considered, such as mobile, immobile, and dipole dislocation configurations; the evolution and dynamic stability of dipolar dislocation arrangements are the main concern. An inherent weakness of this model relates to the neglect of long-range dislocation interactions. This could be a problem with dislocation cell formation where patterning occurs on the same mesoscopic length scale that governs the effective range of dislocation interactions.

In another model, it is assumed that the geometrically necessary effective stress fluctuations experienced by gliding dislocations cause appreciable fluctuations of the local strain rate. This enables the mobile dislocations to probe new configurations again and again. During this process, energetically favorable configurations possess a certain chance to become stabilized, whereas unfavorable arrangements are rapidly dissolved again. Cross slip supports this process by increasing the ''selection pressure.'' That is, through increasing the range of possible slip planes, cross slip increases the efficiency with which dislocations can move down energy gradients. Based on the stochastic dislocation dynamics model from [34], cross slip will increase the fraction of mobile dislocations so the dislocation cell formation is favored by easy cross slip. Figures 5 and 7 show 3D Bragg reflection profiles along the direction cross the shocked line for Al (001) and Al (110) samples. The asymmetric line profile is significant mainly in the range of $\pm 20\ \mu$m from the shocked line center for (110) orientation compared to the $\pm 30\ \mu$m range in (001) orientation. Also, as shown in Fig. 20, the volume of cell wall is less in (110) orientation and has narrower spatial distribution. So, the (001) orientation is easier to form dislocation cell structure than (110) orientation in microscale laser shock peening. As shown in Fig. 21, it is well known for FCC crystals that the plastic slip systems are the {111} family of planes in the ⟨110⟩ family of directions, for a total of 12 possible slip systems. However, the distribution of resolved shear stress in each slip system for loading in different orientations is different [35]. The slip systems that have the maximum resolved shear stresses for loading applied in (001) and (110) orientation samples are shown below, and slip would occur in those slip systems. For the (110) orientation, there are four possible activated slip systems: (111) [10$\bar{1}$], (111) [0$\bar{1}\bar{1}$], ($\bar{1}\bar{1}$1) [011], and ($\bar{1}\bar{1}$1) [101]. For the (001) orientation, there are eight possible activated slip systems: (111) [10$\bar{1}$], (111) [1$\bar{1}$0], ($\bar{1}\bar{1}$1) [10$\bar{1}$], (1$\bar{1}\bar{1}$) [110], ($\bar{1}\bar{1}$1) [110], ($\bar{1}\bar{1}$1) [101], ($\bar{1}\bar{1}$1) [101], and ($\bar{1}\bar{1}$1) [1$\bar{1}$0]. As a result, for the (110) orientation, cross slip is more difficult to occur because there is no common slip direction between different slip planes. However, in (001) orientation, the slip systems (111)⟨101⟩ and ($\bar{1}\bar{1}$1)⟨101⟩ can generate the cross slip between these two slip planes. For the total eight slip systems, cross slip can occur between every two of them. Thus, cross slip is much easier to occur in (001) orientation than in (110) orientation, and this favors the formation of cell structure in (001) orientation.

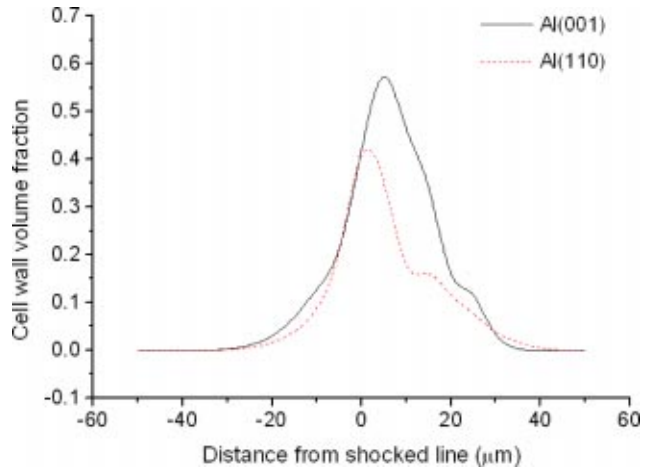

Fig. 20 Volume percentage of cell wall at each measure point for Al (001) and (110)

5 Conclusions

The FEM simulation results and experimental characterization methodologies presented herein enable a systematic study of the microscale laser shock-peening (μLSP) process. The resolved

spatial residual stress and/on strain distribution was achieved in microlevel by X-ray microdiffraction. The compressive residual stress is -80 to -100 MPa within ± 20 μm from the shocked line center, and it decreases very quickly to a few MPa beyond that range. Crystal orientation (001) was found to be more beneficial to the formation of cell structure than (110) orientation. Also, strain deviation at depth direction and average mosaic size were extracted from the recorded X-ray profiles. The lattice rotation field was found to be antisymmetric on the surface across the shocked line. The magnitude of rotation is ± 3 deg and covers a region around ± 35 μm across the shock line center. A mosaiclike substructure was formed in submicron size within the region of ± 20 μm from the shocked line center and consistent with the measurement from EBSD. Strength of the peened region was increased due to the mosaic structure. The experimental results were compared to that from FEM analysis, and the results show a close correspondence between them. Thus, μLSP can be used to improve the reliability performance of microdevices, and the process can be optimized with the above systematic study.

Acknowledgments

This work was supported by the National Science Foundation under Grant No. DMI-02-00334. JWK would like to acknowledge support by the National Science Foundation under the Faculty Early Career Development (CAREER) Program with Grant No. CMS-0134226. Guidance in X-ray microdiffraction provided by Dr. I. Cev Noyan and Dr. Jean Jordan-Sweet is appreciated. Assistance in technical details of sample preparation for EBSD provided by Dr. Yongxue Gang and J. B. Chou is also acknowledged.

References

[1] Walraven, J. A., Mani, S. S., Fleming, J. G., Headley, T. J., Kotula, P. G., Pimentel, A. A., Rye, M. J., Tanner, D. M., and Smith, N. F., 2000, ''Failure Analysis of Tungsten Coated Polysilicon Micromachined Microengines,'' *MEMS Reliability for Critical Applications*, Proc. SPIE, **4180**, pp. 49–57.

[2] Frederick, Kevin M., and Fedder, Gary K., 2000, ''Mechanical Effects of Fatigue and Charge on CMOS MEMS,'' *MEMS Reliability for Critical Applications*, Proc. SPIE, **4180**, pp. 108–116.

[3] Zhang, W., and Yao, Y. L., 2001, ''Feasibility Study of Inducing Desirable Residual Stress Distribution in Laser Micromachining,'' *Trans. North American Manufacturing Research Institution of SME (NAMRC XXIX) 2001*, SME, pp. 413–420.

[4] Zhang, W., and Yao, Y. L., 2000, ''Improvement of Laser Induced Residual Stress Distributions via Shock Waves,'' *Proc. ICALEO'00, Laser Materials Processing*, Detroit, MI, Vol. 89, pp. E183–192.

[5] Zhang, W., and Yao, Y. L., 2000, ''Micro Scale Laser Shock Processing of Metallic Components,'' ASME J. Manuf. Sci. Eng., **124**(2), pp. 369–378.

[6] Chen, H. Q., and Yao, Y. L., 2003, ''Modeling Schemes, Transiency, and Strain Measurement for Microscale Laser Shock Processing,'' *Trans. of The North American Manufacturing Research Institution of SME, NAMRC 31*, Hamilton, Canada, SME, May, pp. 589–596.

[7] Noyan, I. C., Jordan-Sweet, J. L., Liniger, E. G., and Kaldor, S. K., 1998, ''Characterization of Substrate/Thin-Film Interfaces With X-ray Microdiffraction,'' Appl. Phys. Lett., **72**(25), pp. 3338–3340.

[8] Noyan, I. C., Wang, P.-C, Kaldor, S. K., and Jordan-Sweet, J. L., 1999, ''Deformation Field in Single-Crystal Semiconductor Substrates Caused by Metallization Features,'' Appl. Phys. Lett., **74**(16), pp. 2352–2354.

[9] Hutchinson, J. W., 2000, ''Plasticity at the Micron Scale,'' Int. J. Solids Struct., **37**, pp. 225–238.

[10] Clauer, A. H., and Fairland, B. P., 1979, ''Interaction of Laser-Induced Stress Waves With Metals,'' Applications of Lasers in Materials Processing (Ed., E. Metzbower), ASM International, Materials Park, OH, p. 229.

[11] Nalla, R. K., Altenberger, I., Noster, U., Liu, G. Y., Scholtes, B., and Ritchie, R. O., 2003, ''On the Influence of Mechanical Surface Treatments Deep Rolling and Laser Shock Peening on the Fatigue Behavior of Ti-6Al-/4V at Ambient and Elevated Temperatures,'' Mater. Sci. Eng., A, **355**, pp. 216–230.

[12] Fabbro, R., Fournier, J., Ballard, P., Devaux, D., and Virmont, J., 1990, ''Physical Study of Laser-Produced Plasma in Confined Geometry,'' J. Appl. Phys., **68**(2), pp. 775–784.

[13] Asaro, R. J., 1983, ''Micromechanics of Crystals and Polycrystals,'' Adv. Appl. Mech., **23**, pp. 1–115.

[14] Huang, Y., 1991, ''A User-Material Subroutine Incorporating Single Crystal Plasticity in the ABAQUS Finite Element Program,'' Mech Report 178,'' Divi. of Applied Sciences, Harvard Univ., Cambridge, MA.

[15] Kysar, J. W., 1997, Addendum to ''A User-Material Subroutine Incorporating Single Crystal Plasticity in the ABAQUS Finite Element Program,'' Mech Report 178,'' Divi. of Engineering and Applied Sciences, Harvard Univ., Cambridge, MA.

[16] ABAQUS/Standard User's Manual, 2002, Version 6.2, Hibbit, Karlsson, and Sorensen, Inc., Pawtucket, RI.

[17] Rice, J. R., 1987, ''Tensile Crack Tip Fields in Elastic-Ideally Plastic Crystals,'' Mech. Mater., **6**(4), pp. 317–335.

[18] Cullity, B. D., 1978, Elements of X-Ray Diffraction, Second Edition, Addison-Wesley, Reading, MA, London, pp. 268–270.

[19] Noyan, I. C., Wang, P.-C, Kaldor, S. K., and Jordan-Sweet, J. L., 2000, ''Divergence Effects in Monochromatic X-Ray Microdiffraction Using Tapered Capillary Optics,'' Rev. Sci. Instrum., **71**(5), pp. 1991–2000.

[20] SPEC™ X-Ray Diffraction Software, Certified Scientific Software, Cambridge, MA.

[21] *HKL Channel 5™ User's Manual*, 2001, HKL Technology, Danbury, CT.

[22] Chen, H. Q., Kysar, J. W., and Yao, Y. L., 2003, ''Characterization of Plastic Deformation Induced by Micro Scale Laser Shock Peening,'' ASME J. Appl. Mech., (submitted).

[23] Ungar, T., Ribarik, G., Gubicza, J., and Hanak, P., 1984, ''X-Ray Line-Broadening Study of the Dislocation Cell Structure in Deformed [001]-Orientated Copper Single Crystals,'' Acta Metall., **32**(3), pp. 333–342.

[24] Warren, B. E., and Averbach, B. L., 1950, ''The Effect of Cold-Work Distortion on X-Ray Patterns,'' J. Appl. Phys., **21**, pp. 595–599.

[25] Chen, H. Q., Yao, Y. L., and Kysar, J. W., 2003, ''Spatially Resolved Characterization of Residual Stress Induced by Micro Scale Laser Shock Peening,'' *Proc. of 22nd Int. Congress on Applications of Lasers & Electro-Optics (ICALEO)*, Conf. on Laser Materials Processing, Section B, Jacksonville, FL, October, pp. 1–10.

[26] Warren, B. E., 1969, *X-Ray Diffraction*, Addison-Wesley, Reading, MA, Chap. 13.

[27] Noyan, I. C., and Cohen, J. B., 1987, *Residual Stress-Measurement by Diffraction and Interpretation*, Springer-Verlag Inc., New York, pp. 168–175.

[28] Chen, H. Q., Yao, Y. L., Kysar, J. W., Noyan, I. C., and Wang, Y. N., 2003, ''Fourier Analysis of X-Ray Microdiffraction Profiles to Characterize Laser Shock Peened Metals,'' *Trans. of North American Manufacturing Research Institution of SME, NAMRC 32*, Charlotte, NC, June, SME.

[29] Mandel, J., 1982, ''Definition of a Frame Suitable to the Study of Anelastic Transformations of Polycrystal,'' J. Mec. Theor. Appl., **1**(1), pp. 7–23.

[30] Meyers, M. A., Armstrong, R. W., and Kirchner, H., 1999, *Mechanics and Materials: Fundamentals and Linkages*, Wiley, New York, pp. 377–381.

[31] Murr, L. E., 1981, ''Microstructure-Mechanical Property Relations,'' *Shock-Wave and High-Strain-Rate Phenomena in Metals*, Plenum Press, New York, pp. 607–671.

[32] Hansen, N., and Kuhlmann-Wilsdorf, D., 1986, ''Proceedings of the International Conference on Low-Energy Dislocation Structures,'' Mater. Sci. Eng., **81**, pp. 141–152.

[33] Kratochvil, J., 1990, ''Instability Origin of Dislocation Cell Misorientation,'' Scr. Mater., **24**(7), pp. 1225–1228.

[34] Hahner, P., 1996, ''A Theory of Dislocation Cell Formation Based on Stochastic Dislocation Dynamics,'' Acta Mater., **44**(6), pp. 2345–2352.

[35] Stouffer, D. C., and Dame, L. T., 1996, *Inelastic Deformation of Metals*, Wiley, New York, pp. 12–15.